minerals

MDPI

Article

Frankamenite: Relationship between the Crystal–Chemical and Vibrational Properties

Ekaterina Kaneva [1,*], Roman Shendrik [1], Elizaveta Pankrushina [2], Emilia Dokuchits [3], Tatiana Radomskaya [1], Mikhail Pechurin [2] and Aleksey Ushakov [4]

[1] Vinogradov Institute of Geochemistry, Siberian Branch of the Russian Academy of Sciences, Favorsky Str. 1A, Irkutsk 664033, Russia; r.shendrik@gmail.com (R.S.); taniaojigova@mail.ru (T.R.)
[2] Zavaritsky Institute of Geology and Geochemistry, Ural Branch of the Russian Academy of Sciences, Ak. Vonsovsky Str. 15, Ekaterinburg 620110, Russia; lizaveta.94@list.ru (E.P.); mikhail.pechurin@urfu.me (M.P.)
[3] State Key Laboratory of Geological Processes and Mineral Resources, Collaborative Innovation Center for Exploration of Strategic Mineral Resources, School of Earth Resources, China University of Geosciences, Wuhan 430074, China; dokuchits@gmail.com
[4] Mikheev Institute of Metal Physics, Ural Branch of the Russian Academy of Sciences, S. Kovalevskaya Str. 18, Ekaterinburg 620990, Russia; alexushv@mail.ru
* Correspondence: kev604@mail.ru

Abstract: The study provides novel insights into the crystal–chemical and optical characteristics of frankamenite. Frankamenite belongs to a special group (canasite group) of the complex alkaline Ca-(K)-(Na) silicates, and it was found in charoitites from the only known location, Murun Massif, Eastern Siberia, Russia. The crystal–chemical, vibrational, and optical properties of frankamenite were investigated by combining electron probe microanalysis (EPMA), single-crystal X-ray diffraction (SCXRD), infrared (IR) absorption, Raman, UV-Visible absorption, and electron spin resonance (ESR) spectroscopy. The behavior of the peaks in the IR spectra was also studied using ab initio calculations. Detailed characteristics of the internal composition and structure of the mineral species were described, and vibrational and optical properties based on these peculiarities were interpreted. The thermally stimulated reorientation of the H_2O molecules and OH^- groups was studied by thermo-Raman spectroscopy. Octahedral cationic positions can be readily doped with transition metal and lanthanide ions that provide a promising opportunity to adjust the Ce^{3+} luminescence. Hence, frankamenite is a potential material for ion exchange, novel phosphors, and luminophores.

Keywords: frankamenite; crystal chemistry; IR spectroscopy; Raman spectroscopy; ab initio calculation; optical absorption spectroscopy; ESR; luminescence

check for updates

Citation: Kaneva, E.; Shendrik, R.; Pankrushina, E.; Dokuchits, E.; Radomskaya, T.; Pechurin, M.; Ushakov, A. Frankamenite: Relationship between the Crystal–Chemical and Vibrational Properties. *Minerals* **2023**, *13*, 1017. https://doi.org/10.3390/min13081017

Academic Editors: Gligor Jovanovski and Petre Makreski

Received: 15 June 2023
Revised: 18 July 2023
Accepted: 18 July 2023
Published: 29 July 2023

Copyright: © 2023 by the authors. Licensee MDPI, Basel, Switzerland. This article is an open access article distributed under the terms and conditions of the Creative Commons Attribution (CC BY) license (https://creativecommons.org/licenses/by/4.0/).

1. Introduction

Frankamenite, $K_3Na_3Ca_5[Si_{12}O_{30}]F_3(OH)(H_2O)$, is a complex alkaline silicate and unique mineral found today in only one deposit in the world (Murun Massif, Russia). According to the silicate minerals hierarchy of Day and Hawthorne [1], frankamenite is a tube silicate with a one-dimensional tetrahedral polymerization. The $[Si_{12}O_{30}]^{12-}$ -tubes in frankamenite extend along the *c*-axis and consist of two linked ribbons of six-membered rings. This tube is topologically identical to the ${}^3V_{12}$ in the charoite structure (see [2] and therein). The silicon–oxygen radical has the designation ${}^3T_{12}$, where T means "tetrahedron", 3 is the connectivity of the tetrahedron, and 12 is the number of such tetrahedra in the geometrical repeat unit [1]. The tubes are connected to corrugated sheets of Ca^{2+} and Na^+- octahedra parallel to the *c*-axis. The internal channels are occupied by K^+ ions and additional H_2O groups. The silicate tubes and sheets of $(CaO_4(OH)F)^{8-}$- and $(NaO_4F_2)^{9-}$-octahedra occur in layers, alternating along the *c*-axis.

The same type of tube (${}^3T_{12}$) can be found in the crystal structures of canasite [3] and fluorcanasite [4], insofar as frankamenite is the triclinic polymorph of the above minerals.

Canasite contains four $(OH)^-$ sites, while in fluorcanasite there are two F sites, an (OH) site, and a mixed (F,OH) site, all of which are bound to the Na^+ and Ca^{2+}-octahedra.

The minerals of the canasite group are listed for comparison in Table 1. The crystal structure of canasite, discovered in the Khibiny Massif in the 1950s, has been determined over several decades [5,6] and was successfully refined by Rozhdestvenskaya et al. in 1988 [3]. They also noted differences in the chemical compositions of the canasite minerals from the Khibiny and Murun Massifs [3], the latter of which was also characterized by Evdokimov and Regir in 1994 [7]. In 1992, Nikishova et al. presented the results of crystal structure refinement of the mineral from Yakutian charoitites (Murun Massif), calling it triclinic canasite [8]. The structure of this variety was refined within the space group *P*1, which explained the difficulties [3] encountered while working with these samples and the presence of additional reflections in the diffraction patterns. The crystal structure and interatomic distances slightly differ from those of monoclinic canasite from the Khibiny Massif. In 1994, triclinic canasite was approved by the CNMNC as a new mineral called frankamenite [9]. It was named after the Russian mineralogist and crystallographer, professor of St. Petersburg State University, V.A. Frank-Kamenetsky. An interesting fact is that charoite was also initially mistaken for lilac canasite, but after a detailed study, it became recognized as another mineral species [10]. The last paper on the refinement of its structural features was published in 1996 [11]. In 2003, Rastsvetaeva et al. [12] reported on canasite from the Khibiny Massif containing a high content of fluorine. This species differs from canasite in symmetry (space group *Cm* vs. *C*2/*m* of canasite) and occupancies of the octahedral positions. These characteristics enabled its approval in 2007 by the CNMNC as a new mineral called fluorcanasite [4]. According to [12], fluorcanasite can be considered either as a fluorine analogue of canasite or as a monoclinic analogue of frankamenite. The intensity of studies of minerals of the canasite group has noticeably declined over the past 15 years, despite the fact that, for example, the optical and vibrational properties of frankamenite are yet to be studied.

Table 1. Canasite group minerals.

Mineral	Ideal Structural Formula [1]	Type Locality	Sp. gr.
Canasite	$K_3Na_3Ca_5[Si_{12}O_{30}](OH)_4$	Khibiny Massif	*C*2/*m*
Frankamenite	$K_3Na_3Ca_5[Si_{12}O_{30}]F_3(OH)(H_2O)$	Murun Massif	*P*1
Fluorcanasite	$K_3Na_3Ca_5[Si_{12}O_{30}]F_3(OH)(H_2O)$	Khibiny Massif	*Cm*

Deciphering and interpreting the vibrational modes of frankamenite remain questionable. However, having structural data (*P*1 (No. 1), point group C_1 (1)), it is possible to calculate a set of phonon modes in the center of the Brillouin zone based on factor–group analysis [13]: Γ = 183A (using https://www.cryst.ehu.es/rep/sam.html (accessed on 15 June 2023)). The latter indicates the polarity of the frankamenite crystal.

Within the last few decades, canasite-based materials have received unprecedented interest. These compounds are potential glass–ceramic materials. Glass–ceramics are polycrystalline solids obtained by the controlled crystallization of glass during a heat treatment process that contain one or several crystalline phases, and in most cases, a residual glassy phase. Bioactive silicate glass–ceramics can be used as long-term implants due to their relatively high mechanical strength and only negligible and slow solubility of silicates in human body fluids [14]. Studies concerning the development of glass–ceramics, which are potentially suitable for biomedical applications, have reported that CaO, P_2O_5, and F, regardless of their origin, must be the essential compositional components of glass–ceramic systems ([15] and therein). One of the potential glass–ceramic materials is canasite [16]. The stoichiometric canasite forms a stable glass, requiring only a few percent excess fluoride to achieve efficient nucleation, and it is easy to produce essentially monophase glass–ceramics [17].

According to [18], an ideal osteoconductive bioglass–ceramic should be free of Al_2O_3. Fluorcanasite (with composition $K_2Na_4Ca_5Si_{12}O_{30}F_4$) glass–ceramics were obtained by controlling the glass crystallization in the SiO_2–K_2O–Na_2O–CaO–CaF_2 system [19]. Bandyopadhyay-Ghosh et al. (2010) [20] reported modified fluorcanasite glass–ceramic compositions based on changing the Na_2O and CaO molar ratios and adding P_2O_5.

Due to good castability combined with excellent cell response in vitro, modified fluorcanasites have great potential for use as load-bearing, osteoconductive biomaterials in orthopedics, implantology, and reconstructive facial surgery [18,20,21], whereas stoichiometric fluorcanasite glass–ceramics showed poor mechanical properties and crumbled during mechanical processing [22]. By modifying the compositions, the biological activity of the modified glass–ceramics can be significantly increased [23,24]. The addition of lithium disilicate increases the chemical resistance of fluorcanasite-based glass–ceramics [25,26]. Vyas et al. (2022) [27] found out that with increased fluorcanasite content in the composition, hydrophilicity also increases over the entire surface of the sample, and, subsequently, cell adhesion and proliferation is raised.

Fluorcanasite glass–ceramics have excellent mechanical properties [28]. The type, size, and volume ratio of the primary crystalline phases in the material directly affect the properties of canasite-based glass–ceramics [29]. Phase evolution in canasite-based compositions is complex, and small compositional modifications significantly change the crystallizing product and the nucleation mechanism [30]. The main crystalline phases are canasite and frankamenite, often having an interpenetrating lattice structure [31]. At relatively low temperatures, frankamenite predominantly nucleates homogeneously throughout the glass [30]. According to published data [30,31], the nucleation temperature for the phases of the canasite group is ~520 °C, and the temperature of crystal growth is ~780 °C.

Glass–ceramics find applications in cookware, hermetic sealing, and electronic substrates, among others. One of the applications of glass–ceramics is for sealing solid oxide fuel cell (SOFC) components, mainly using alkaline earth-metal-based aluminosilicate glass–ceramics [32].

It is important to understand that in order to create such relevant modern materials, the widest possible knowledge of the compounds used is necessary. Recently, Kaneva et al. (2021) [33] made the first attempt to study the vibrational properties of this mineral. However, the data are only descriptive. This work reveals new insights into the crystal–chemical and optical properties of frankamenite.

2. Materials and Methods

2.1. Sample Description

The studied frankamenite sample was taken from the Murun Massif (Malyy Murun), Aldan Shield, Siberia, Russia. Frankamenite is associated with charoite, pectolite, microcline, aegirine, tinaksite, and quartz [7]. The mineral forms flattened, rosette-shaped or radial–radiant aggregates and can have different colors: from gray, bluish, and lilac-gray to greenish and brown (Figure 1).

Moreover, frankamenite is an unusual collectible stone, and its presence in a sample along with charoite, which is a well-known and visually very attractive gem material, as well as various associated minerals, creates an interesting appearance [34].

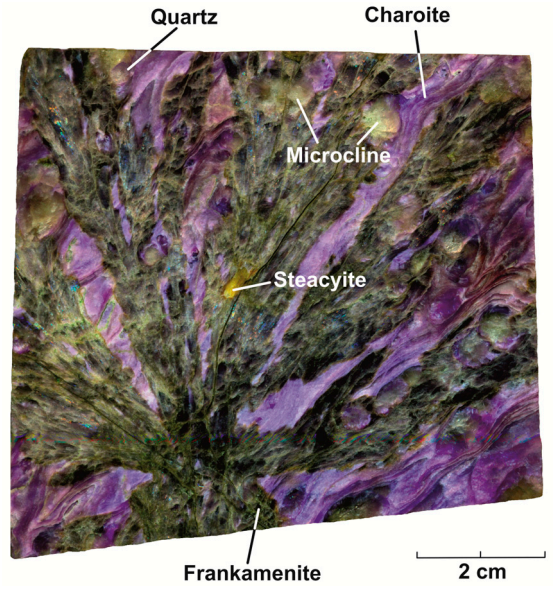


Figure 1. A sample of charoitite with frankamenite (Murun Massif, Aldan Shield, Siberia, Russia).

2.2. Crystal–Chemical Analysis

Mineral compositions were analyzed with a JEOL JXA-8230 Electron Probe Microanalyzer (Jeol, Tokyo, Japan) equipped with five wavelength-dispersive spectrometers (WDS) (Jeol, Tokyo, Japan). The samples were firstly coated with a thin conductive carbon film prior to analysis. The precautions suggested by [35] were used to minimize the difference of carbon film thickness between samples and obtain an approx. 20 nm uniform coating. Operating conditions for quantitative WDS analyses involved an accelerating voltage of 15 kV, a beam current of 5 nA, and a 20 μm spot size. Data were corrected online using a ZAF (atomic number, absorption, fluorescence) correction procedure. The content of H_2O was calculated by difference and then involved into the ZAF correction procedure. The peak counting time was 10 s for Ca, Mg, K, F, Si, Al, Fe, Na, Sr, and Ba and 20 s for Ti and Mn. The background counting time was 1/2 of the peak counting time on the high- and low-energy background positions. The following standards were used: diopside (Ca, Mg), sanidine (K), fluorite (F), olivine (Si), jadeite (Na), rhodonite (Mn), SrF_2(Sr), pyrope garnet (Al, Fe), and barite (Ba). Electron probe microanalysis (EPMA) results (determined over 8 spots) obtained for the studied frankamenite sample are reported in Table 2. The atom proportions in atoms per formula units (apfu) were derived on the basis of 12 Si + Al cations.

Table 2. Average chemical composition (wt.%) for the studied frankamenite crystal.

Constituent	wt.%	Range	Stand. Dev.	Atom	apfu
SiO_2	55.78	54.81–57.19	0.15	Si	11.99
Al_2O_3	0.04	0–0.29	0.05	Al	0.01
Na_2O	6.57	6.09–6.91	0.26	Na	2.74
MgO	0.01	0–0.03	0.01	Mg	–
K_2O	10.82	10.62–11.08	0.14	K	2.97
CaO	21.83	21.45–22.15	0.21	Ca	5.03
MnO	0.42	0.34–0.48	0.04	Mn	0.08
FeO	0.07	0.03–0.12	0.04	Fe	0.01
SrO	0.28	0.17–0.39	0.06	Sr	0.03
BaO	0.10	0–0.26	0.09	Ba	0.01
F	4.41	4.30–4.61	0.16	F	3.00
Sum	100.33				
–O=F2	1.86				
H_2O	1.56				
Total	100.03				

The crystal structure of the frankamenite sample was studied using a Bruker AXS D8 VENTURE automated diffractometer equipped with a four-circle Kappa goniometer, a CCD detector, and monochromatized MoK*a* radiation. The operating conditions were 50 kV and 1 mA. The detector-to-crystal working distance was 40 mm. The collection strategy was optimized with the APEX2 (Bruker AXS Inc, Berlin, Germany) suite package [36]. A combination of several ω and ϕ rotation sets was used for the recording of the entire Ewald sphere (±h, ±k, ±l) up to θ_{max} ~33°. The extraction of the reflection intensities and the correction of the Lorenz polarization effect was carried out with the SAINT package [37]. The SADABS software was provided for a semi-empirical absorption correction [38], and the XPREP [39] was used for the calculation of the intensity statistics. The crystal structure was refined in the space group *P*1 using the CRYSTALS program [40]. The twin operation has been identified with the ROTAX program [41] with the following matrix [101, −1−1−0.5, 00–1]. The refined parameters were scale factor, atom positions, anisotropic/isotropic displacement parameters, and extra-Si-framework cations' occupancies. Occupancies for Si and O atoms were constrained to 1. In [8], the designation "M" was used to denote octahedral positions with mixed occupancies of Ca and Na, numbered from 1 to 8. This nomenclature was employed in our study. For the refinement of the Ca and Na occupancies in the M-octahedra the restrain Ca + Na = 1 ± 0.01 was imposed. The results of X-ray diffraction study of the frankamenite sample could not be used to locate H atoms of OH groups and water molecules. The quality of the crystals was not good; after several attempts at data collection, the reported one was found to be the best.

Initial fractional coordinates and atom labeling were taken from [10]. The summary data regarding the single crystals, the data-collection parameters, and the structural refinements are given in Table 3, whereas final atomic coordinates, site occupancies, and equivalent displacement parameters are reported in Table S1 of Supplementary Materials. Selected interatomic distances and angles are given in Tables S2 and S3 of Supplementary Materials, respectively.

Table 3. Selected data on single crystal, data collection, and structure refinement parameters of the studied frankamenite.

Crystal Data			
a (Å)	10.093(1)	*α* (°)	89.954(4)
b (Å)	12.695(1)	*β* (°)	111.043(4)
c (Å)	7.2347(8)	*γ* (°)	110.244(4)
V (Å^3)	803.6(2)	Space group, *Z*	*P*1, 1
Crystal dimensions (mm)		0.194 × 0.089 × 0.046	
Data collection		**Refinement**	
Reflections measured	40,780	Reflections used in the refinement (I > $3\sigma_{(I)}$)	7437
Independent reflections	11,451	No. of refined parameters	515
$R_{merging}$ ($R_{(int)}$) (%)	4.28	*R* [a] (on *F*) (%)	3.67
h_{min}, h_{max}	−15, 15	R_w [b] (on *F*) (%)	4.75
k_{min}, k_{max}	−19, 19	Goof [c]	1.0653
l_{min}, l_{max}	−10, 11	$\Delta\rho_{min}/\Delta\rho_{max}$ (e$^-$/Å^3)	−0.48/0.61
$Theta_{min}/Theta_{max}$	2.328/32.883	Twin element ratio	0.496:0.504

[a] $R = \Sigma[|F_o| - |F_c|]/\Sigma|F_o|$. [b] $R_w = [\Sigma[w(F_o^2 - F_c^2)^2]/\Sigma[w(F_o^2)^2]]^{1/2}$; *w*—Chebyshev optimized weights. [c] Goodness-of-Fit = $[\Sigma[w(F_o^2 - F_c^2)^2]/(N - p)]^{1/2}$, where *N* and *p* are the number of reflections and parameters, respectively.

The CIF was deposited with the Cambridge Crystallographic Data Centre (CCDC 2171487).

A statistical analysis of structural data was performed using the calculation of the coordination polyhedra characteristics. In this analysis, we applied the calculations of the parameters earlier described in [42]. The geometric parameter calculation as a measure of polyhedral irregularity was based on the centroid method developed by [43]. A computer program (IVTON) which calculates these parameters is available [44]. Bond valence calculation (Table S4 of Supplementary Materials) was performed using the parameters obtained by [45] and [46]. The figures showing structural details were prepared using the program VESTA (version 4.3.3, Tsukaba, Kyoto, Japan) [47].

2.3. Ab Initio Calculations

Ab initio calculations of the frankamenite crystal structure were performed using the density functional theory (DFT) [48] that was implemented in the VASP package [49]. The projector augmented wave (PAW) with the exchange–correlation functional in Perdew–Burker–Ernzerhof (PBE) [50] in the generalized gradient approximation (GGA) was used to construct the basis wave functions. The cutoff energy threshold for these potentials was chosen to be E cutoff = 600 eV. Integration during iterative matching was performed over a uniformly distributed grid of $4 \times 3 \times 2$ k-points throughout the Brillouin zone. The crystal structure in the GGA calculations was preliminarily relaxed to an interatomic force value $\geq$0.005 eV/A. The phonon spectra were calculated at the center of the Brillouin zone (Γ) in a similar GGA approximation.

2.4. Infrared Spectroscopy

Infrared spectra were measured with a Fourier-Transform Infrared (FTIR) spectrometer FT-801 (Simex, Novosibirsk, Russia). The powdered samples were mixed with anhydrous KBr, pelletized, and analyzed in the range of 480–4000 cm^{-1} at a resolution of 2 cm^{-1}, and 32 were collected for each spectrum. The FTIR spectrum of an analogous pellet of pure KBr was used as a reference. The mixed and pelletized sample was heated at different temperatures to study the frankamenite dehydration. The methodology was described in [51].

2.5. Raman Spectroscopy

Raman spectra in the range of 20–4000 cm^{-1} were measured in the Common Use Center "Geoanalitik" using a Horiba LabRam HR800 Evolution equipped with an Olympus BX-FM confocal microscope, He-Ne laser (radiation wavelength 633 nm, laser power of 4 mW), and a Linkam TSM 600 heating/cooling stage to study in situ Raman spectra in the temperature range of −190–600 °C; no photoluminescence was observed with this excitation. An Olympus 50× objective (numerical aperture = 0.7) was used. The acquisition time was 20–30 s, with 2 accumulations per spectral segment. The diffraction grating of 1800 gr/mm and an electrically cooled charge-coupled device detector were used to record the spectra. The spectrometer calibration was guided along the Rayleigh line and the emission lines of a neon lamp. The re-equipment and comprehensive development of the "Geoanalitik" shared research facilities of the IGG UB RAS is financially supported by the grant of the Ministry of Science and Higher Education of the Russian Federation (Agreement No. 075-15-2021-680).

2.6. Optical Spectroscopy and ESR

The photoluminescence and excitation spectra were registered at room temperature using a LS-55 spectrofluorimeter (Perkin-Elmer, Valencia, CA, USA). The optical absorption spectrum was measured on the frankamenite plate with thickness of approx. 1 mm using a Lambda-950 spectrophotometer (Perkin-Elmer, CA, USA). Electron Spin Resonance spectrum was recorded using RE-1306 radiospectrometer 6 (KBST, Yartsevo, Russia) operated at a microwave frequency of 9380 MHz.

3. Results

3.1. Crystal Chemistry and Structure Description

Chemical analyses of frankamenite published earlier in the literature have been combined in [52]. The atom proportions in atoms per formula units (apfu) for studied frankamenite are reported in Table 2. The composition of our frankamenite in relation to Na_2O and CaO is almost identical to that of the other Murun samples reported in [52]. There is a higher K_2O content in relation to previously published analyses. The content of F in the literature ranges from 3.72 to 5.75 wt.%, while the content of F in our sample has a range of 4.30–4.61 wt.%.

Considering the results of electron probe microanalysis and crystal structure refined, the following crystal–chemical formula can be proposed for the studied frankamenite: $K_{2.97}Ba_{0.01}Na_{2.74}Ca_{5.03}Mn_{0.08}Sr_{0.03}Fe_{0.01}[Si_{11.99}Al_{0.01}O_{30}](F_3(OH))\cdot 0.64H_2O$.

The projection of crystal structure along the *a*-axis is shown in Figure 2.

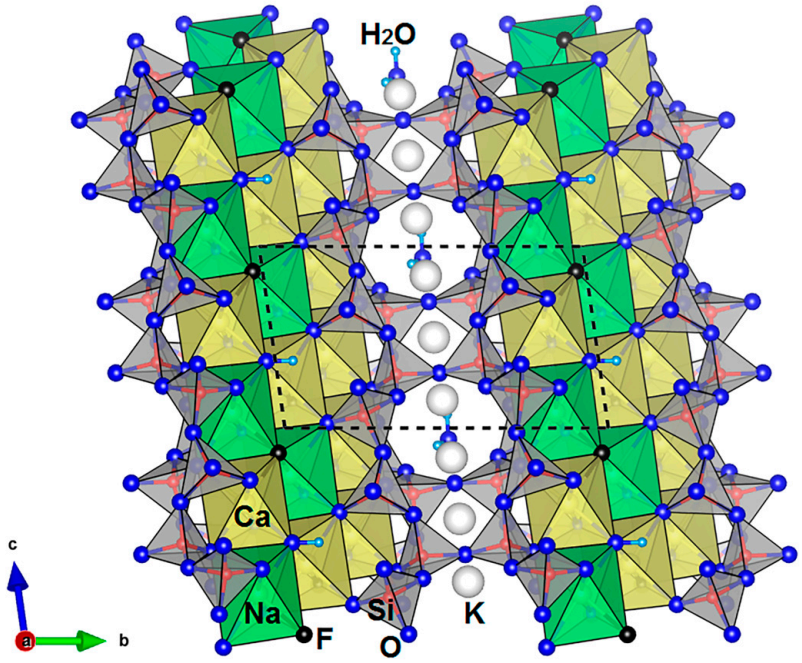


Figure 2. The frankamenite crystal structure, as viewed down the *a*-axis. The unit cell is shown.

When analyzing the geometric structural characteristics of the frankamenite model refined, we used several significant parameters to identify the degree of distortion. They were calculated and are listed in Table 4. Using the centroid method, where the centroid is defined as the point in the coordination polyhedron having the minimum variance of the distances to the vertices, we may obtain the parameters defining the displacement of the central atom from its ligands (r_v, Δ_V, r_s, Δ, Table 4). The volume eccentricity (ECCv) and the volume sphericity (SPHv) describe the displacement of the central atom from its ligands and the deviation of vertices of a polyhedron from the surface of a best-fit sphere to the ligand positions, respectively. Bond length distortion (BLD) is a measure of the dispersion of the individual bond lengths, and the bond angle variance (TAV and OAV) is a measure of the dispersion of the individual angle. The quadratic elongation (TQE and OQE) is dimensionless and equal to 1 for a regular polyhedron, while for a distorted polyhedron, it is >1.

Table 4. Calculated geometrical and distortion parameters for polyhedra in the crystal structure of the studied frankamenite sample: ECoN—effective coordination number [47,53,54], Vp—volume of the coordination polyhedron [43,44], r—average experimental distance from the cation to the ligands (see Table S2 of Supplementary Materials), r_v—average distance from the volume center to the ligands [43,44], Δ_V—distance of the central atom to the volume center [43,44], r_s—average distance from the centroid to the ligands [43,44], Δ—distance of the central atom to the centroid [43,44], Vs—volume of the sphere fitted to the positions of ligands [43,44], ECCv—volume eccentricity [43,44], SPHv—volume sphericity [43,44], BLD—bond length distortion [47,55,56], A—average experimental ligand–central atom–ligand angle (see Table S2 of Supplementary Materials), TAV—tetrahedral angle variance [47,56], TQE—tetrahedral quadratic elongation [47,56], OAV—octahedral angle variance [47,56], OQE—octahedral quadratic elongation [47,56].

	Si1	**Si2**	**Si3**	**Si4**	**Si5**	**Si6**
ECoN	3.916	3.996	3.906	3.924	3.823	3.966
Vp (Å^3)	2.119	2.117	2.261	2.200	2.068	2.170
r (Å)	1.608	1.609	1.644	1.626	1.596	1.621
r_v (Å)	1.606	1.608	1.642	1.625	1.593	1.620
Δ_V (Å)	0.061	0.016	0.063	0.059	0.081	0.040
r_s (Å)	1.605	1.606	1.641	1.625	1.593	1.618
Δ (Å)	0.100	0.087	0.104	0.071	0.112	0.096
Vs (Å^3)	17.362	17.423	18.554	17.989	16.941	17.818
ECCv	0.1090	0.0293	0.1112	0.1050	0.1450	0.0724
SPHv	0.9999	0.9999	1.0000	0.9999	1.0000	0.9999
BLD (%)	1.79	0.47	2.01	1.93	2.59	1.23
A (°)	109.3	109.3	109.4	109.4	109.3	109.3
TAV	22.747	24.649	27.532	10.076	28.264	23.021
TQE	1.005	1.006	1.007	1.003	1.007	1.006
	Si7	**Si8**	**Si9**	**Si10**	**Si11**	**Si12**
ECoN	3.901	3.935	3.967	3.947	3.972	3.970
Vp (Å^3)	2.197	2.239	2.090	2.137	2.211	2.183
r (Å)	1.628	1.639	1.601	1.616	1.630	1.626
r_v (Å)	1.625	1.637	1.599	1.614	1.629	1.625
Δ_V (Å)	0.072	0.059	0.039	0.048	0.038	0.043
r_s (Å)	1.625	1.635	1.598	1.611	1.628	1.622
Δ (Å)	0.099	0.115	0.095	0.129	0.083	0.099
Vs (Å^3)	17.982	18.362	17.122	17.597	18.114	17.987
ECCv	0.1271	0.1046	0.0717	0.0874	0.0687	0.0766
SPHv	0.9999	1.0000	0.9999	1.0000	0.9999	1.0000
BLD (%)	1.99	1.62	1.19	1.50	1.12	1.25
A (°)	109.3	109.3	109.3	109.2	109.4	109.3
TAV	21.892	28.672	21.739	45.552	17.988	29.384
TQE	1.005	1.007	1.005	1.010	1.004	1.007
	M1	**M2**	**M3**	**M4**	**M5**	**M6**
ECoN	5.983	5.984	5.965	5.929	5.966	5.956
Vp (Å^3)	18.912	17.442	17.787	17.225	17.023	17.769
r (Å)	2.438	2.368	2.392	2.372	2.362	2.392
r_v (Å)	2.438	2.368	2.391	2.373	2.363	2.392
Δ_V (Å)	0.023	0.030	0.046	0.049	0.045	0.010
r_s (Å)	2.438	2.367	2.391	2.370	2.359	2.390
Δ (Å)	0.031	0.020	0.074	0.084	0.084	0.071
Vs (Å^3)	60.678	55.608	57.251	55.970	55.250	57.335
ECCv	0.0286	0.0372	0.0568	0.0608	0.0564	0.0121
SPHv	0.9779	0.9872	0.9818	0.9602	0.9791	0.9546
BLD (%)	0.78	0.67	1.13	1.06	1.00	1.18
A (°)	90.0	90.0	90.0	90.1	90.1	89.9
OAV	46.555	31.905	54.943	73.448	71.895	56.354
OQE	1.014	1.010	1.017	1.022	1.021	1.018

Table 4. *Cont.*

	M7	M8	K1	K2	K3
ECoN	5.893	5.990	8.947	9.017	8.651
Vp (Å^3)	17.248	16.944	49.004	50.087	50.491
r (Å)	2.373	2.357	3.100	2.978	2.980
r_v (Å)	2.373	2.358	3.098	2.987	2.980
Δ_V (Å)	0.049	0.021	0.067	0.103	0.024
r_s (Å)	2.370	2.355	3.075	2.969	2.966
Δ (Å)	0.098	0.095	0.355	0.186	0.256
Vs (Å^3)	55.986	54.890	124.499	111.606	110.834
ECCv	0.0609	0.0270	0.0632	0.1003	0.0237
SPHv	0.9455	0.9864	0.9804	0.8517	0.8525
BLD (%)	1.77	0.44	1.17	3.63	3.55
A (°)	90.1	90.0	–	–	–
OAV	72.134	70.168	–	–	–
OQE	1.022	1.020	–	–	–

Average tetrahedra distances for Si1–Si12 lie within 1.60(2)–1.64(1) Å (Table S2 of Supplementary Materials); the measured Si–O individual distances range from 1.513(9) to 1.692(7) Å (Table S2 of Supplementary Materials). The differences between the experimental values and the calculated rv and rs values do not exceed 0.005 Å, and they lie within the estimated standard deviations range. A relatively low BLD values of parameter, not exceeding 3%, indicate that the tetrahedral bond lengths are closely grouped around an average value. The quadratic elongations (TQEs) are in the range of 1.003–1.010, which means that the tetrahedra are distorted. Indeed, the high values of the TAV parameters (10.076–45.552) confirmed this. The eccentricity (circle has eccentricity = 0, ellipses have an eccentricity of less than 1) ranges from ~0.07 to ~0.15 for Si-tetrahedra, and the sphericity (it is less than 1 for non-spherical objects) is equal to 0.9999 or 1.0000.

Information about the coordination numbers for cation and anion positions and BVS values are represented in Table S4 of Supplementary Materials. Relevant information about the cation site population and mean atomic number are given in Table 5. A satisfactory agreement between the mean electron numbers and the average interatomic distances (Table 5 and Table S2 of Supplementary Materials), as derived by X-ray and EPMA measurements, was found. The <cation–anion> distance (r, Table 4) and the volume (Vp) of the M1 and M8 octahedra are the largest and the smallest, respectively. This provided grounds to distribute ions with an ionic radius greater than those of Ca and Na (according to [57]) into the M1 position and ions with an ionic radius smaller than those of Ca and Na into the M8 position (Table 5). The calculated average distances from the volume center to the ligands and from the centroid to the ligands deviated a little from the experimental values of the average distances from the cation to the ligands: −0.000–0.003 Å. It should be noted that the crystal structure exhibiting the octahedra sites was also lightly distorted. The main differences in the M-octahedra distortion parameters involve the OAV parameter, which ranges from ~46.6 to ~73.5. The eccentricity achieves 0.061, and the sphericity is much less than 1 (to 0.94). Generally, OQE parameters of octahedra are very similar.

The distortion parameters for the K sites (Table 4) are generally higher than those of other polyhedra of the crystal structure. The K2 site exhibits the greatest volume eccentricity value, and for the volume sphericity, the more distorted is the K1 site.

Table 5. Polyhedral cation distribution and mean atomic numbers (m.a.n., e^-) of cation sites, as determined by structure refinement (X-ray) and chemical analysis (EPMA).

Site	This Study				[10]	
	Cation Distribution	$e^-_{X\text{-ray}}$	e^-_{EPMA}	Δe^-	Cation Distribution	e^-
K1	$K_{0.99}$	18.20	18.81	0.61	$K_{0.87}$	16.53
K2	$K_{0.99}$	18.38	18.81	0.43	K	19.00
K3	$K_{0.99}Ba_{0.01}$	19.82	19.37	0.45	K	19.00
M1	$Na_{0.85}Ca_{0.10}Sr_{0.03}$	12.87	12.49	0.38	Na	11.00
M2	$Ca_{0.99}$	20.00	19.80	0.20	Ca	20.00
M3	$Ca_{0.56}Na_{0.43}$	16.20	15.93	0.27	$Na_{0.52}Ca_{0.48}$	15.32
M4	$Ca_{0.76}Na_{0.23}$	18.04	17.73	0.31	$Ca_{0.54}Na_{0.46}$	15.86
M5	$Ca_{0.73}Na_{0.25}$	17.81	17.35	0.46	$Ca_{0.70}Na_{0.30}$	17.30
M6	$Ca_{0.56}Na_{0.43}$	16.25	15.93	0.32	$Ca_{0.69}Na_{0.31}$	17.21
M7	$Ca_{0.75}Na_{0.23}$	17.99	17.53	0.46	$Ca_{0.73}Na_{0.27}$	17.57
M8	$Ca_{0.58}Na_{0.32}Mn_{0.08}Fe_{0.01}$	17.72	17.38	0.34	$Ca_{0.72}Na_{0.28}$	17.48

3.2. Ab Initio Calculations

The calculated phonon spectrum of frankamenite considering the data on its structure presented in this paper allows us to define the full vibrational representation as Γ = 183A. According to the ab initio calculations, frankamenite was found to be characterized by vibrations with the following frequencies: four modes corresponding to vibrations of the water region and OH-radicals at ~3490–3722 cm^{-1} and one mode characterizing the H–O–H vibrations of water ~1585 cm^{-1}. The other modes can be conditionally divided into three spectral groups of vibrations of the silicon–oxygen framework: 53–546 cm^{-1} (126 modes), 576–789 cm^{-1} (21 modes), and 895–1108 cm^{-1} (31 modes). A detailed analysis of the vibrations of the crystal according to the DFT data showed the predominant vibration of the Si–O rings and is discussed in detail below.

3.3. Infrared and Raman Spectroscopy

The absorption and Raman spectra of frankamenite are given in Figures 3 and 4.

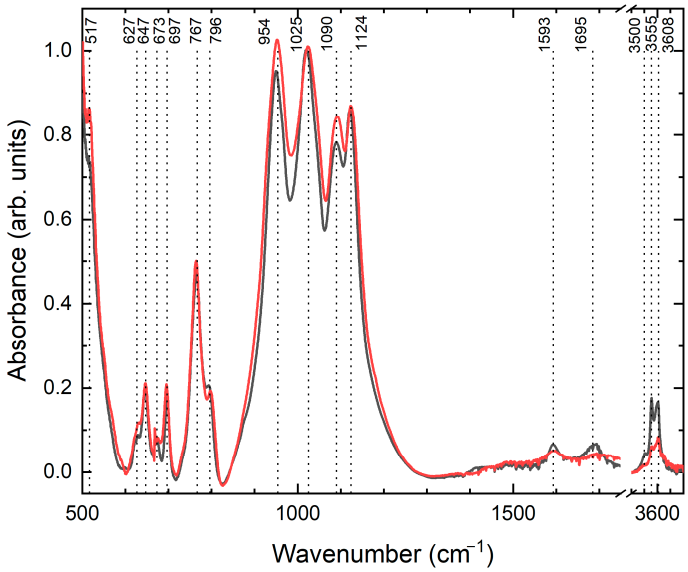


Figure 3. Infrared absorption spectra of frankamenite before (black curve) and after (red curve) heating at 700 °C.

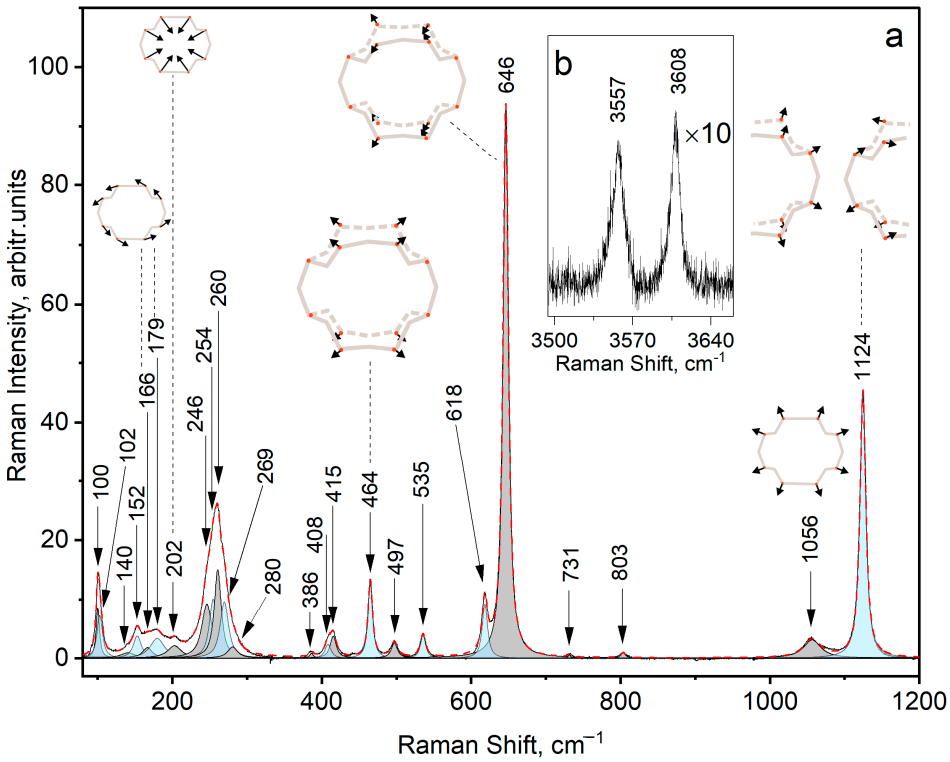


Figure 4. Raman spectra of frankamenite at 25 °C (**a**). In insert (**b**), water and OH vibrations are shown.

In view of the polarity of the crystal (all the presented vibrations are active both in IR and in Raman scattering), further consideration was carried out, as presented together in Table 6. As noted above, all frankamenite vibrations should be characterized as ring vibrations of the Si–O-framework in the *ab* plane, which does not allow interpretation of this in terms of the external and internal vibrations (like ν1–4). The ring vibrations of the Si–O-framework are proposed to be classified into three types according to DFT calculation. There are symmetrical ring motion vibrations that are active in the 517–1090 cm^{-1} region (Table 6, Figure 5) in IR and in the 166–1056 cm^{-1} region (Table 6, Figure 6) in the Raman spectra. The asymmetrical ring motion appeared at ~647, 697 cm^{-1} (Figure 5) in IR and at ~415, 464, 646, and 731 cm^{-1} (Figure 6) in the Raman spectra. The semiring motion-attributed bands are located at 1124 cm^{-1} (Figure 5) in IR and at ~803, 1124 cm^{-1} (Figure 6) in the Raman spectra. The breathing modes located at 166, 179, and 1056 cm^{-1} and the ring rotation around the *c*-axis at 202 and 954 cm^{-1} could also be separated.

Table 6. Raman and infrared band positions and suggested assignments of the observed bands in frankamenite.

Raman Modes, cm^{-1}	IR Modes, cm^{-1}	Assignment
415, 464, 646, 731	647, 697	Asymmetrical ring motion
166, 179, 1056		Breathing modes
202	954	Ring rotation around the *c*-axis
166, 179, 202, 246, 254, 260, 269, 280, 386, 497, 535, 618, 1056	517, 627, 673, 767, 796, 964, 1025, 1090	Symmetrical ring motion
	1593, 1695	Bending H–O–H
3557	3500, 3555	Stretching H–O–H modes (ν_1 and ν_3)
3608	3608	Stretching O–H vibrations (ν_1).

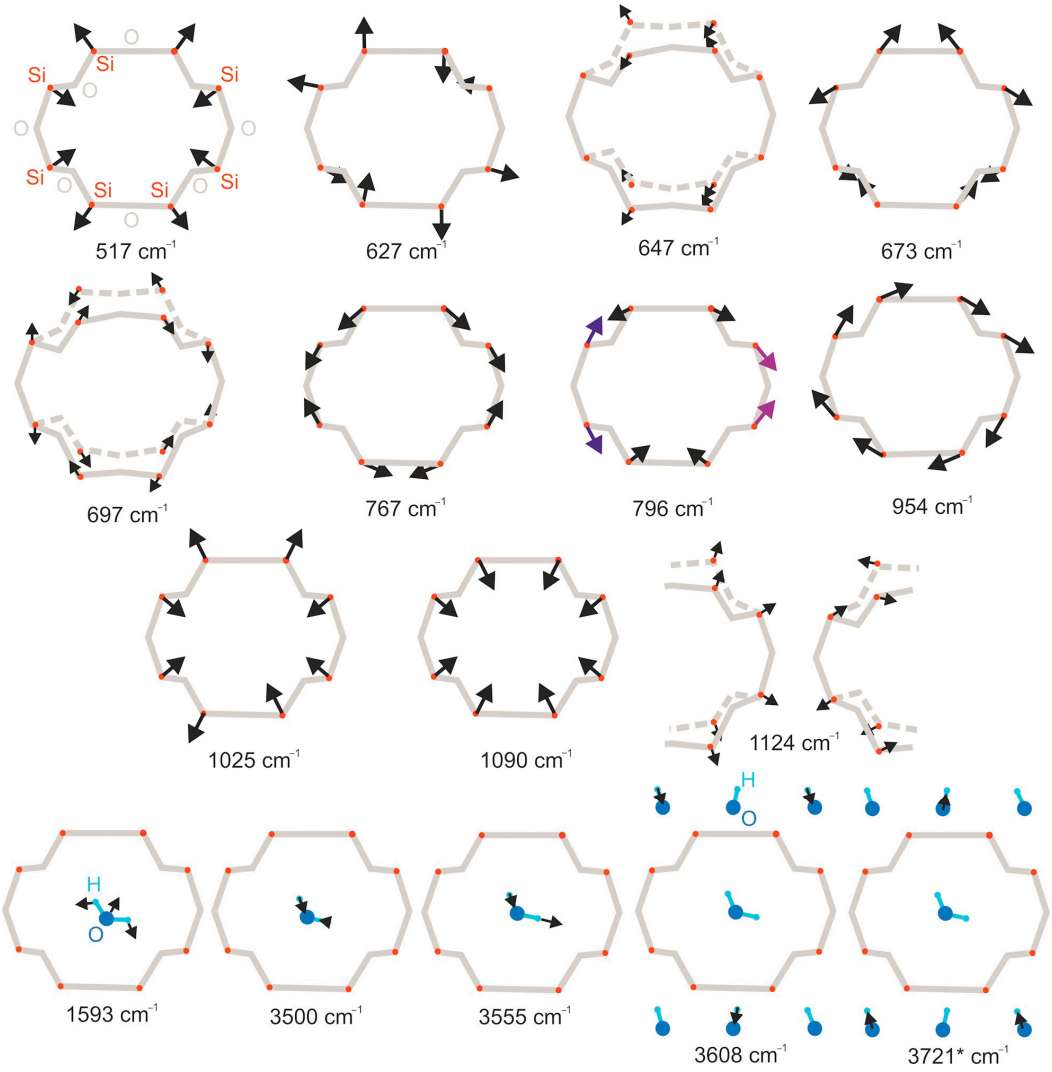


Figure 5. The schematic image (according to DFT data) of the Si–O-framework vibrations registered experimentally according to IR spectroscopy data. The 3721 (*) cm^{-1} vibration was not experimentally registered (the peak position according to DFT).

The bands located at 1593 and 1695 cm^{-1} correspond to bending H–O–H modes. According to the DFT calculation, the vibration of ~1695 cm^{-1} was not observed. The peaks at 3500 and 3557 cm^{-1} are related to stretching H–O–H modes (ν_1 and ν_3), and 3608 cm^{-1} is related to stretching O–H vibrations (ν_1).

The infrared spectrum of frankamenite did not change significantly after heating the sample. The bands at 796 and 954 cm^{-1} were slightly shifted. However, the intensities of bands at 3500 and 3555 cm^{-1} were decreased in the temperature interval of 250–600 °C. The temperature dependencies of integral absorbance for these bands are given in Figure 7.

No phase transitions were detected in the temperature range of −190–600 °C. The only significant structural change is the transformation of water at ~−150 °C and its further structural loss during heating.

An interesting observation is the behavior of the $\nu_3(H_2O)$ and $\nu_1(OH)$ modes. The $\nu_3(H_2O)$ during cooling in the temperature range from 30 to −70 °C undergoes a decrease in relative intensity with respect to the $\nu_1(OH)$ mode, which subsequently remains stable in this temperature range. In the range from −70 to −190 °C, an increase in the intensity of $\nu_3(H_2O)$ was observed again (Figure 8b). I$\nu_3(H_2O)$ is approximated by the sine function (Figure 9). The $\nu_1(OH)$ mode remains stable upon cooling to −110 °C, and, subsequently, a

significant decrease in the relative intensity was observed at lower temperatures, while at −190 °C, it is hardly observed.

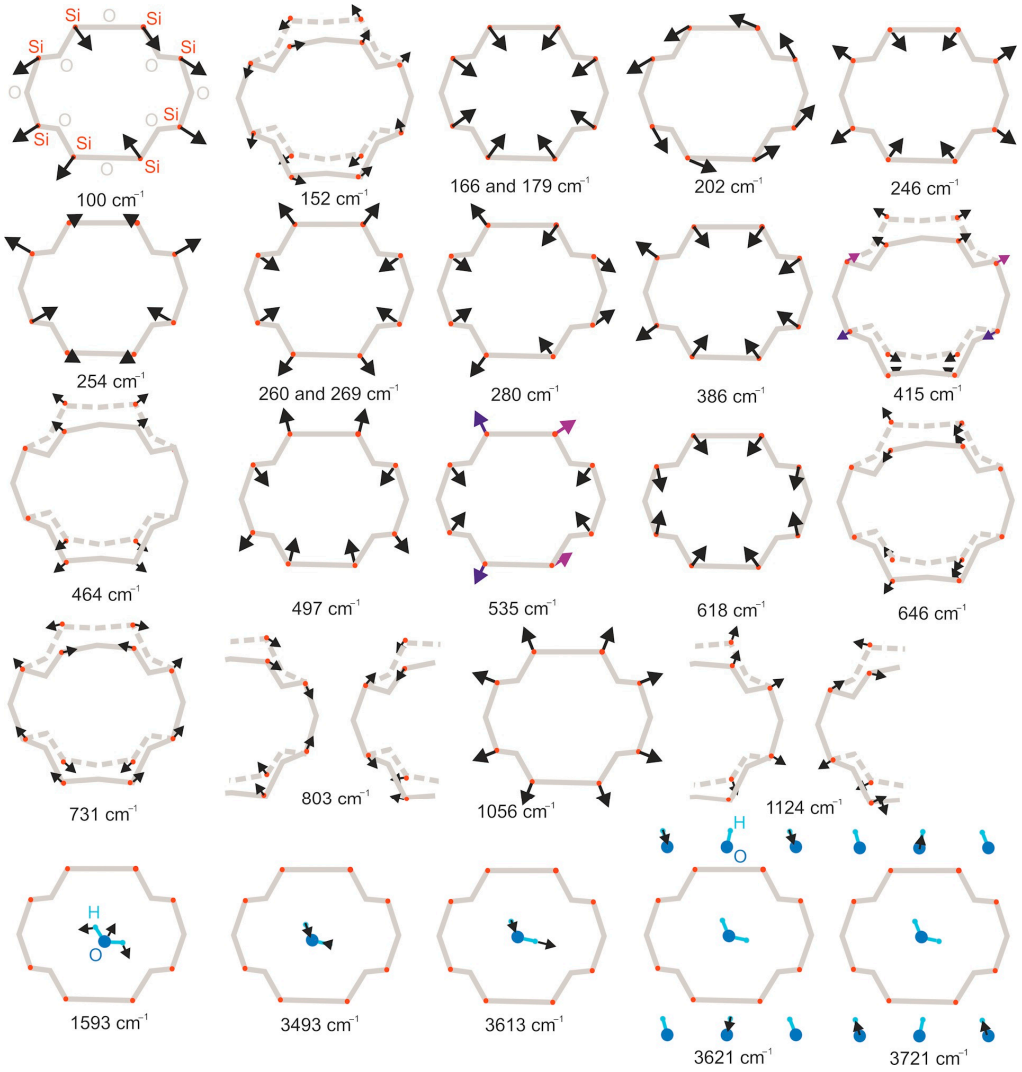


Figure 6. The schematic image (according to DFT data) of the Si–O-framework vibrations registered experimentally according to Raman spectroscopy data. The 1593, 3493, and 3721 (*) cm^{-1} vibrations were not experimentally registered (the peak positions according to DFT).

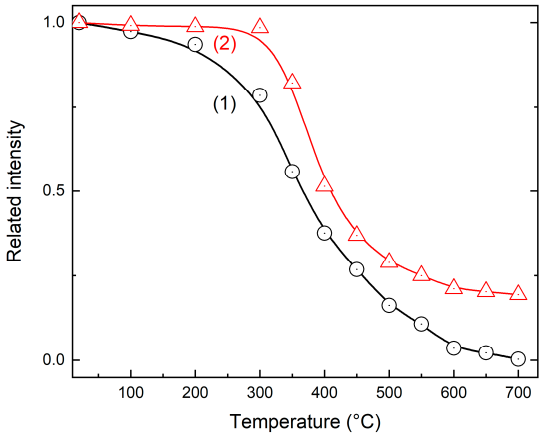


Figure 7. Temperature dependencies of integral absorbance of 3500 cm^{-1} (curve (1)) and 3555 cm^{-1} (curve (2)).

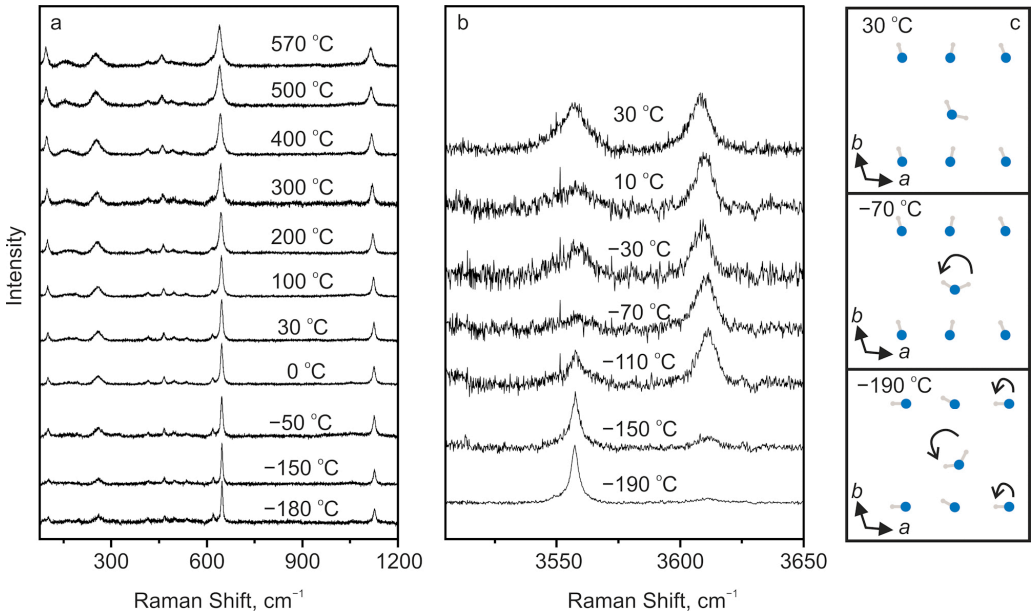


Figure 8. The evolution of the frankamenite Raman spectra in the spectral range of 80–1200 cm^{-1} from −190 to 570 °C (**a**) and in the spectral range of 3500–3650 cm^{-1} from −190 to 30 °C (**b**); (**c**) a schematic image of the H_2O and OH-reorientation during cooling.

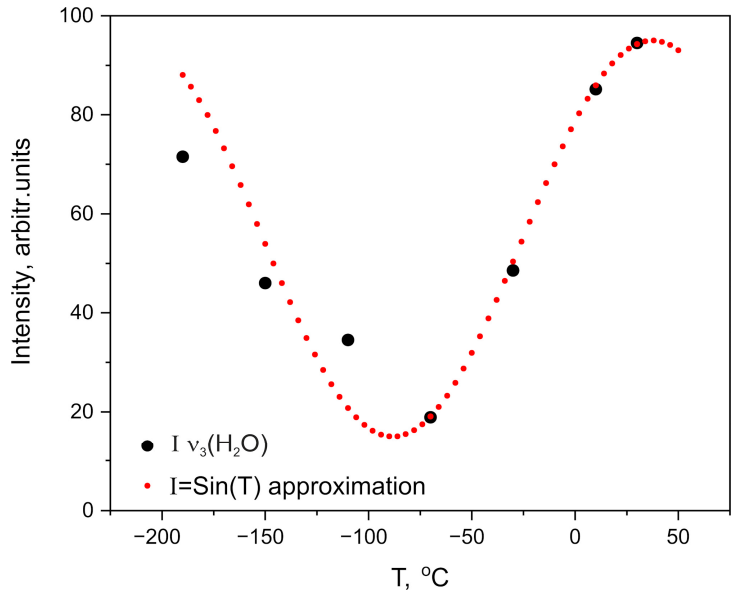


Figure 9. The dependence of ν3(H_2O) spectral peak intensity on temperature (T = −190–30 °C). Red dotted line is approximation of sine function.

3.4. Optical Absorption and Luminescence

The absorption spectrum of frankamenite sample is given in Figure 10. The absorption bands peaked at 377, 416, and 439 nm are attributed to the forbidden $^6A_1$ to $^4A_1$, ^4E; $^4T_2$; and $^4T_1$ transitions in Mn^{2+} ions. The photoluminescence wide band peaking at 500 nm is found under excitation (Figure 11). The presence of Mn^{2+} ions was also detected using the ESR technique. The characteristic sextet was found in the studied sample.

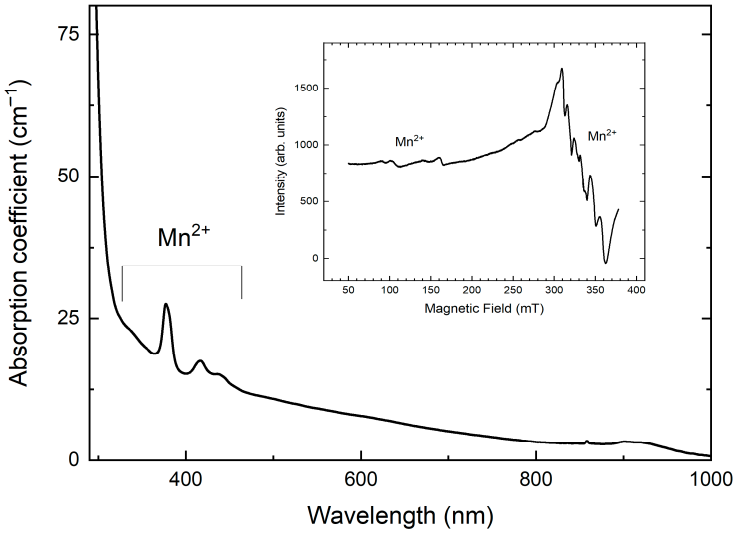


Figure 10. The UV/Vis/NIR absorption spectrum of frankamenite. ESR spectrum measured at room temperature is shown in the insert.

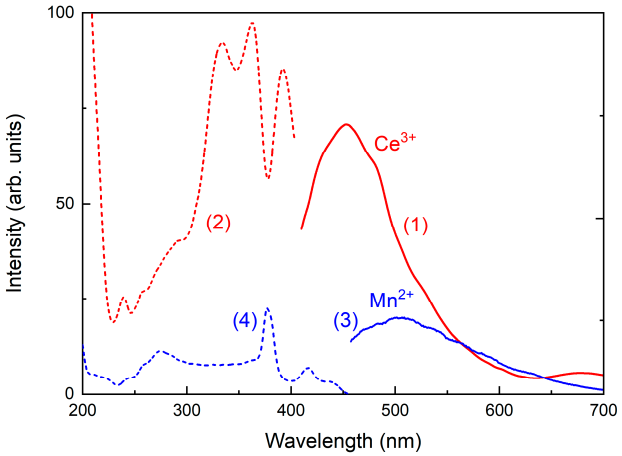


Figure 11. Luminescence and excitation spectra of frankamenite measured at room temperature: (1) luminescence spectrum under 370 nm excitation; (2) excitation spectrum monitored at 430 nm; (3) luminescence spectrum under 416 nm excitation; (4) excitation spectrum monitored at 520 nm.

The intense luminescence band at 450 nm is observed under excitation at 390 nm (Figure 11). This luminescence is attributed to 5d-4f transitions in Ce^{3+} ions.

4. Discussion

In the crystal structure of minerals belonging to the canasite group, listed in Table 1, the $^{3}T_{12}$ tubes [1] connect to ridged sheets of M-octahedra (occupied by Ca^{2+} and Na^{+}) and alternate along the *c*-axis. Inside each tube, there are K^{+} ions and an additional (H_2O) group. In the crystal structure of frankamenite and canasite [3], there are three positions of K atoms, while in fluorcanasite, one of the three positions is split into two around the center of symmetry [12]. Canasite has four (OH) sites [3], frankamenite has two F and two (OH) sites, while fluorcanasite has two F sites, an (OH) site, and a mixed site that usually contains more F than (OH) [12]. All of these sites are bonded to *M*-octahedra. Frankamenite (sp. gr. *P*1) contains eight independent octahedral positions (Table 5), while canasite (sp. gr. *C*2/*m*) and fluorcanasite (sp. gr. *Cm*) crystal structure has six *M*-sites. In frankamenite, one *M*-site is occupied by Na, one position is filled by Ca, and the remaining octahedral positions are occupied simultaneously by Na and Ca. Fluorcanasite has two Na positions, three Ca sites, and a mixed Na+Ca position [12]. According to the data in [3], in the crystal structure of canasite, Ca is ordered over four positions, while Na occupies the

remaining two M-positions. Thus, the minerals of the canasite group exhibit significant crystal chemical differences, expressed primarily in symmetry and chemical composition, and they occupy M-octahedral sites and positions of additional anions while having a similar $[Si_{12}O_{30}]^{12-}$ tube tetrahedral framework.

The results and atomic coordinates of the simulated crystal structure model of frankamenite are reported in Table S5 of Supplementary Materials. It is interesting to compare the geometric and distortion parameters of the initial crystal structure of natural frankamenite and simulated structural model (Table S6 of Supplementary Materials).

It should be noted that the Si–O values for Si-tetrahedra in the model do not exhibit significant deviations (0.31–2.51%, Table S6 of Supplementary Materials). Effective coordination numbers of Si-tetrahedra have minor deviations from the experimental ones: 0.03–3.63%. The average deviations of the tetrahedron volume and volume of the sphere fitted to the positions of the vertices of the tetrahedron are 3.4%. The above parameters of deviations for M-octahedra are slightly higher: <cation–anion> distance deviation = 0.08–3.78%, mean deviation for M1–M8 octahedra volumes and fitted sphere volumes are 4.38 and 4.61%, respectively, and ECoN deviation = 4.12%, which is the average of eight M-octahedra. The largest deviations in geometrical parameters are noted for K-polyhedra (ECoN and Vp values, Table S6 of Supplementary Materials). However, for r and Vs values, the deviations lay in the ranges of 0.13–2.11 and 1.64–5.53%, respectively, except for a few single values of deviation that do not exceed 16%. In general, it can be concluded that the simulated structural model is very close to the experimentally obtained model of the natural frankamenite crystal structure. Moreover, in the optimized crystal structure model, the coordinates of the H positions for the hydroxyl groups and water molecules are established.

The two types of channels are distinguished inside the crystal structure of frankamenite. Channel I is extended along the *c*-axis and delimited by the eight-membered rings of tetrahedra (Figure 12a). The shortest distances between oppositely located oxygen atoms in the ring are 7.435(8) × 6.066(10) Å. Channel II is delimited by the eight-membered tetrahedral rings along the *a*-axis (Figure 12b). The ring cross section has free diameters of 4.793(9) × 4.134(7) Å. The *effective channel width* (*ecw*)—defined as the distance between the oxygen atoms in the smallest *n*-ring or the smallest free aperture subtracted by 2.7 Å when the oxygen ionic radius is assumed to be 1.35 Å [58]—for channel I is 4.74 × 3.37 Å, and for channel II, it is 2.09 × 1.43 Å. According to [59], a minimum *ecw* of 3.2 Å is required for a crystalline substance to be defined as microporous. In the frankamenite structure, only channel I is suitable for this parameter. The pores inside this channel of frankamenite have larger dimensions with respect to the channel aperture and, therefore, theoretically may contain guest atoms larger than K and water molecules, occupying these cavities in the natural mineral.

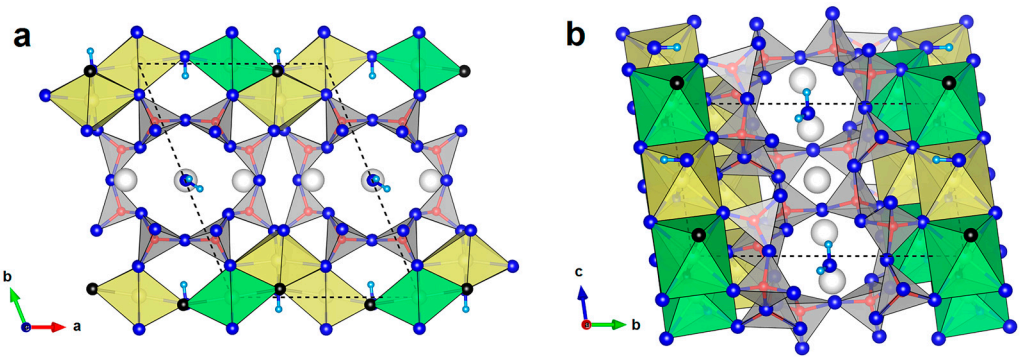


Figure 12. A perspective view of the frankamenite crystal structure fragments projected down the *c*-axis with aperture of channel I (**a**) and down the *a*-axis with an aperture of channel II (**b**). The atom designation is the same as in Figure 2.

In the FTIR spectra of frankamenite, the three bands attributed to O–H stretching modes at 3500, 3555, and 3608 cm^{-1} were found (Figure 3). According to the Libowitzky

equations [60], the O···O distances corresponding to these bands are 2.90 Å and 3.00 Å. The O···H distances are approximately 2.05, 2.15, and 2.55 Å. Beckenkampet al. (1992) [61] proposed the equation for the determination of the shortest distance from OH-anion to metal. Following this equation, the distances attributed to the absorption bands at 3608 cm^{-1} are equal to 2.40 Å, which is close to the distance between metal and OH given in Table S2 of Supplementary Materials. Therefore, the band at 3698 cm^{-1} could be attributed to two types of OH-anions in frankamenite. The bands at 3500 and 3555 cm^{-1} are decreased when heated. The aperture of channel I is larger than that of channel II. The water molecules could easily move within channel I (Figure 12), and dehydration occurs there at a lower temperature than within channel II [51,62].

According to the general concepts, the polarized spectra maintain a constant relationship between the intensity of any mode and the orientation of the corresponding chemical bond in the crystal [63]. H_2O molecules and OH-radicals at 30 °C are predominantly oriented along the crystallographic direction *b* (schematic image in Figure 8c). Apparently, H_2O molecules undergo rotation when the crystal is cooled (one of the supposed schemes of H_2O reorientation is shown in Figure 8). At T = −70 °C, $\nu_3(H_2O)$ are characterized by the lowest relative intensity (Figures 8b and 9), which presumably indicates the orientation of the H_2O molecule orthogonal to the laser polarization vector. The subsequent increase in $I\nu_3$ (H_2O) indicates the continued rotation of the molecule. OH-radicals reorient in a similar way; however, their turn to the position orthogonal to the polarization vector occurs at lower temperatures (at ~−150 °C). The latter is likely due to the peculiarities and unequal environments of H_2O and OH (as mentioned above).

The Ce^{3+} may substitute Ca^{2+} ions in the M3–M8 positions. The average energies of the Ce^{3+} f-d transitions in the silicates containing polyhedral layers of Ca cations correlate with the average cation–oxygen distance (Figure 13). Taking into account the observed cation and anion distribution, the following isomorphous substitution scheme could be suggested for frankamenite: $Ca^{2+} + OH^- / F^- \leftrightarrow Ce^{3+} + O^{2-}$ or $2Ca^{2+} + O^{2-} \leftrightarrow Ce^{3+} + \square + OH^-$.

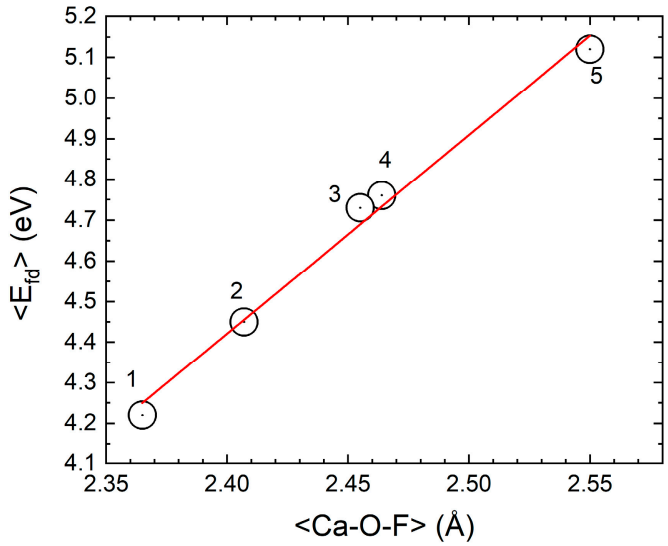


Figure 13. Correlation between cation–oxygen distances and the average energies of Ce^{3+} f-d transitions in the silicates in the complex alkaline silicates containing Ca-polyhedral layers: 1—frankamenite from this article; 2—fedorite [42]; 3—carletonite [64]; 4—fluorcarletonite [64]; 5—agrellite [65].

Frankamenite contains cationic positions (M sites) that can be easily doped with transition metal (e.g., Mn^{2+}, Cr^{3+}, Fe^{2+}, Fe^{3+}) and lanthanide ions with other average energy of f-d transitions that could be useful for the tuning of Ce^{3+} luminescence. Therefore, frankamenite could be a prospective material for ion exchanger, novel phosphors, and luminophores.

5. Conclusions

In this study, the crystal–chemical and optical properties of frankamenite, a member of the canasite group, were examined in detail. This rare and unique alkaline silicate mineral is currently only known to exist in the Murun Massif deposit (Russia). A comprehensive crystal–chemical analysis was conducted on mineral samples, and for the first time, the optical and vibrational properties of frankamenite were investigated. The crystal–chemical formula of frankamenite is $K_{2.97}Ba_{0.01}Na_{2.74}Ca_{5.03}Mn_{0.08}Sr_{0.03}Fe_{0.01}[Si_{11.99}Al_{0.01}O_{30}](F_3(OH))\cdot 0.64H_2O$.

In the crystal structure of compound, the $[Si_{12}O_{30}]^{12-}$ tetrahedral tubes are connected to M-octahedral sheets, alternating along the *c*-axis. There are eight independent octahedral positions in frankamenite, and the site population of each position has been proposed based on chemical and structural studies. The pores within the channels of frankamenite structure have larger dimensions compared with the channel apertures. As a result, the mineral has the potential to contain additional guest atoms and groups (such as K or water molecules), which can move within the channel during heating. In fact, dehydration of frankamenite occurs at temperatures above 250 °C. Thermo-Raman spectroscopy detected the thermally induced reorientation of H_2O molecules and OH^- groups in the structure of frankamenite.

Furthermore, optical absorption and luminescence investigations revealed that Mn^{2+} and Ce^{3+} ions may substitute Ca^{2+} ions in the M3–M8 positions of frankamenite. Consequently, the cationic positions (M sites) in frankamenite can easily be doped with transition metal and lanthanide ions. As a result, frankamenite holds potential as a material for ion exchange, novel phosphors, and luminophores.

Thus, the data obtained in this work show that, in addition to glass–ceramic production, the mineral frankamenite is a promising material for the use of compounds based on its crystal chemistry in the research field of photonics. The results also demonstrated the significant potential of utilizing ab initio calculations in the examination of natural compounds. Through the integration of SCXRD, EMPA, and Raman and IR spectroscopy techniques, alongside ab initio calculations, a comprehensive analysis of the material's spectroscopic features can be carried out, accounting for its structural characteristics.

Supplementary Materials: The following supporting information can be downloaded at https://www.mdpi.com/article/10.3390/min13081017/s1, Table S1: Crystallographic coordinates, occupancies, and equivalent/isotropic atomic displacement parameters (Å2) of the frankamenite sample, Table S2: Selected bond distances (Å) for tetrahedra and polyhedra of the studied frankamenite sample, Table S3: Selected angles (°) for tetrahedra and polyhedra of the studied frankamenite sample, Table S4: Bond–valence sum (BVS) and coordination number (CN) of the cation and anion structural positions for the studied frankamenite sample, Table S5: Crystallographic coordinates of the simulated structural model of frankamenite, Table S6: Calculated geometrical and distortion parameters for polyhedra in the simulated structure model of frankamenite [43,44,47,53–56].

Author Contributions: Conceptualization, E.K. and R.S.; methodology, E.K., R.S. and E.P.; software, M.P., E.P. and A.U.; validation, E.K. and E.D.; formal analysis, E.K. and R.S.; investigation, E.K., R.S., E.P. and E.D.; writing—original draft preparation, E.K., R.S. and E.P.; writing—review and editing, E.K. and E.D.; visualization, E.K., T.R., E.P. and R.S.; supervision, E.K.; project administration, E.K. All authors have read and agreed to the published version of the manuscript.

Funding: The crystal structure, infrared, optical absorption, and luminescence studies were supported by the Russian Science Foundation (Project No. 22–27–00183, https://rscf.ru/project/22-27-00183/) (accessed on 15 June 2023). The electron probe microanalysis of frankamenite was supported by the National Natural Science Foundation of China Project (No. 42050410318).

Data Availability Statement: Not applicable.

Acknowledgments: The crystal structure research was performed at the "Baikal analytical center for collective use" at the Favorsky Irkutsk Institute of Chemistry SB RAS. The optical and luminescence studies were carried out using facilities of the Vinogradov Institute of Geochemistry SB RAS. Raman spectra were measured in the Common Use Center "Geoanalitik" at the Zavaritsky Institute of Geology and Geochemistry UB RAS (program 123011800012-9). The electron probe microanalysis was carried out at the Laboratory of Microscopy and Microanalysis at the Wuhan Microbeam Analysis Technology Co., Ltd. Ab initio calculations were performed using the Supercomputer of the Mikheev Institute of Metal Physics UB RAS (program 122021000038-7 (Quantum)). We are grateful to reviewers for their valuable comments.

Conflicts of Interest: The authors declare no conflict of interest.

References

1. Day, M.; Hawthorne, F.C. A structure hierarchy for silicate minerals: Chain, ribbon, and tube silicates. *Mineral. Mag.* **2020**, *84*, 165–244. [CrossRef]
2. Rozhdestvenskaya, I.; Mugnaioli, E.; Czank, M.; Depmeier, W.; Kolb, U.; Merlino, S. Essential features of the polytypic charoite-96 structure compared to charoite-90. *Mineral. Mag.* **2011**, *75*, 2833–2846. [CrossRef]
3. Rozhdestvenskaya, I.V.; Nikishova, L.V.; Bannova, I.I.; Lazebnik, Y.D. Canasite: Refinement of structure and structural typomorphism. *Miner. Zh.* **1988**, *10*, 31–44. (In Russian)
4. Khomyakov, A.P.; Nechelyustov, G.N.; Krivokoneva, G.K.; Rastsvetaeva, R.K.; Rozenberg, K.A.; Rozhdestvenskaya, I.V. Fluorcanasite, $K_3Na_3Ca_5Si_{12}O_{30}(F,OH)_4 \cdot H_2O$, a new mineral species from the Khibiny alkaline pluton, Kola peninsula, Russia, and new data on canasite. *Geol. Ore Depos.* **2009**, *51*, 757–766. [CrossRef]
5. Dorfman, M.D.; Rogachev, D.L.; Goroshchenko, Z.I.; Uspenskaya, E.I. Canasite: A new mineral. *Tr. Mineral. Muzeya Akad. Nauk SSSR.* **1959**, *9*, 158–166. (In Russian)
6. Chiragov, M.I.; Mamedov, K.S.; Belov, N.V. Crystal structure of canasite, $Ca_5Na_4K_2[Si_{12}O_{30}](OH,F)_4$. *Dokl. Akad. Nauk SSSR.* **1969**, *185*, 672–674. (In Russian)
7. Evdokimov, M.D.; Regir, E.P. Canasite in charoite of the Murun alkaline complex (Sirenevy Kamen deposit). *Zap. Vseross. Mineral. O-va* **1994**, *123*, 104–118. (In Russian)
8. Nikishova, L.V.; Lazebnik, K.A.; Rozhdestvenskaya, I.V.; Emel'yanova, N.N.; Lazebnik, Y.D. Triclinic canasite from charoitites of Yakutia. *Mineral. Zh.* **1992**, *14*, 71–77. (In Russian)
9. Nikishova, L.V.; Lazebnik, K.A.; Rozhdestvenskaya, I.V.; Emel'yanova, N.N.; Lazebnik, Y.D. Frankamenite $K_3Na_3Ca_5(Si_{12}O_{30})F_3(OH)\cdot nH_2O$—A new mineral species. Triclinic analogue of canasite from charoitite. *Zap. Vseross. Mineral. O-va* **1996**, *125*, 106–108. (In Russian)
10. Konev, A.A.; Vorob'ev, E.I.; Lazebnik, K.A. *Mineralogy of the Alkaline Murun Massif*; SB RAS, SPC JIGGM: Novosibirsk, Russia, 1996. (In Russian)
11. Rozhdestvenskaya, I.V.; Nikishova, L.V.; Lazebnik, K.A. The crystal structure of frankamenite. *Mineral. Mag.* **1996**, *60*, 897–905. [CrossRef]
12. Rastsvetaeva, R.K.; Rozenberg, K.A.; Khomyakov, A.P.; Rozhdestvenskaya, I.V. Crystal structure of F-canasite. *Dokl. Chem.* **2003**, *391*, 177–180. [CrossRef]
13. Kroumova, E.; Aroyo, M.I.; Perez-Mato, J.M.; Kirov, A.; Capillas, C.; Ivantchev, S.; Wondratschek, H. Bilbao Crystallographic Server: Useful Databases and Tools for Phase-Transition Studies. *Phase Transit. A Multinat. J.* **2003**, *76*, 155–170. [CrossRef]
14. Farag, M.M.; El-Rashedi, A.M.I.; Rüssel, C. In vitro biocompatibility evaluation of canasite-calcium phosphate glass-ceramics. *J. Non-Cryst. Solids* **2018**, *488*, 24–35. [CrossRef]
15. Basaran, N.; Capoglu, A. The effect of LiF, CaF_2 and MgF_2 addition on the sintering and crystallisation behaviour of a base glass containing calcined bone ash. *J. Non-Cryst. Solids* **2021**, *561*, 120752. [CrossRef]
16. Miller, C.A.; Kokubo, T.; Reaney, I.M.; Hatton, P.V.; James, P.F. Formation of apatite layers on modified canasite glass–ceramics in simulated body fluid. *J. Biomed. Mater. Res.–B Appl. Biomater.* **2002**, *59*, 473–480. [CrossRef]
17. El-Meliegy, E.; van Noort, R. Models of Bioactive Glass Ceramics. In *Glasses and Glass Ceramics for Medical Applications*; Springer: New York, NY, USA, 2012; pp. 229–238. [CrossRef]
18. Bandyopadhyay-Ghosh, S.; Reaney, I.M.; Hurrell-Gillingham, K.; Brook, I.M.; Hatton, P.V. Evaluation of modified fluorcanasite glass-ceramics for bone tissue augmentation. *Key Eng. Mater.* **2005**, *284–286*, 557–560. [CrossRef]
19. Johnson, A.; Shareef, M.Y.; Van Noort, R.; Walsh, J.M. Effect of furnace type and ceramming heat treatment conditions on the biaxial flexural strength of a canasite glass-ceramic. *Dent. Mater.* **2000**, *16*, 280–284. [CrossRef]
20. Bandyopadhyay-Ghosh, S.; Faria, P.E.P.; Johnson, A.; Felipucci, D.N.B.; Reaney, I.M.; Salata, L.A.; Brook, I.M.; Hatton, P.V. Osteoconductivity of modified fluorcanasite glass–ceramics for bone tissue augmentation and repair. *J. Biomed. Mater. Res. A* **2010**, *94*, 760–768. [CrossRef]
21. Kraipok, A.; Intawin, P.; Kamnoy, M.; Bintachitt, P.; Leenakul, W.; Panyata, S.; Eitssayeam, S.; Tunkasiri, T.; Pengpat, K. Preparation and characterization of lithium disilicate-fluorcanasite glass-ceramics for dental applications. *J. Mech. Behav. Biomed. Mater.* **2023**, *137*, 105548. [CrossRef]

22. Kanchanarat, N.; Bandyopadhyay-Ghosh, S.; Reaney, I.M.; Brook, I.M.; Hatton, P.V. Microstructure and mechanical properties of fluorcanasite glass-ceramics for biomedical applications. *J. Mater. Sci.* **2008**, *43*, 759–765. [CrossRef]
23. Omar, A.A.; Hamzawy, E.M.A.; Farag, M.M. Crystallization of fluorcanasite–fluorrichterite glasses. *Ceram. Int.* **2009**, *35*, 301–307. [CrossRef]
24. Vyas, A.; Vijay Kumawat, S.; Bandhu Ghosh, S.; Bandyopadhyay-Ghosh, S. Microstructural analysis and bioactive response of selectively engineered glass-ceramics in simulated body fluid. *Mater. Technol.* **2020**, *36*, 451–459. [CrossRef]
25. Abo-Mosallam, H.A.; Mahdy, E.A. Crystallization behavior and properties of fluorcanasite–lithium disilicate glasses for potential use in dental application. *Ceram. Int.* **2019**, *45*, 21144–21149. [CrossRef]
26. Kraipok, A.; Intawin, P.; Bintachitt, P.; Leenakul, W.; Khamman, O.; Eitssayeam, S.; Tunkasiri, T.; Pengpat, K. Influence of heat treatment temperature on the properties of the lithium disilicate-fluorcanasite glass-ceramics. *Int. J. Appl. Ceram.* **2022**, *19*, 1415–1427. [CrossRef]
27. Vyas, A.; Bandhu Ghosh, S.; Bandyopadhyay-Ghosh, S.; Agrawal, A.K.; Khare, D.; Dubey, A.K. Digital light processing mediated 3D printing of biocomposite bone scaffolds: Physico-chemical interactions and in-vitro biocompatibility. *Polym. Compos.* **2022**, *43*, 3175–3188. [CrossRef]
28. Takav, P.; Banijamali, S.; Sedaghat Ahangari Hossein Zadeh, A.; Mobasherpour, I. Influence of TiO_2 content on phase evolution, microstructure and properties of fluorcanasite glass-ceramics prepared through sintering procedure for dental restoration applications. *Ceram. Int.* **2018**, *44*, 7057–7066. [CrossRef]
29. Cheng, J.; Deng, W.; Zheng, W.; Tian, P.; Lin, M.; Ji, S. Phase transition of different crystals in canasite-based glass-ceramics. *J. Chin. Ceram. Soc.* **2012**, *40*, 1415–1419.
30. Kanchanarat, N.; Miller, C.A.; Hatton, P.V.; James, P.F.; Reaney, I.M. Early stages of crystallization in canasite-based glass ceramics. *J. Am. Ceram.* **2005**, *88*, 3198–3204. [CrossRef]
31. Bandyopadhyay-Ghosh, S.; Reaney, I.M.; Brook, I.M.; Hurrell-Gillingham, K.; Johnson, A.; Hatton, P.V. In vitro biocompatibility of fluorcanasite glass-ceramics for bone tissue repair. *J. Biomed. Mater. Res. A* **2007**, *80*, 175–183. [CrossRef]
32. Ananthanarayanan, A.; Tricot, G.; Kothiyal, G.P.; Montagne, L. A comparative overview of glass-ceramic characterization by MAS-NMR and XRD. *Crit. Rev. Solid State Mater. Sci.* **2011**, *36*, 229–241. [CrossRef]
33. Kaneva, E.V.; Shendrik, R.Y.; Vladykin, N.V.; Radomskaya, T.A. Crystal-chemical features of rare and complex silicates from charoite rocks of the Malyy Murun volcano-plutonic alkaline complex. In *Alkaline Rocks, Kimberlites and Carbonatites: Geochemistry and Genesis. Springer Proceedings in Earth and Environmental Sciences*; Vladykin, N., Ed.; Springer: Cham, Switzerland, 2021; pp. 115–129. [CrossRef]
34. Hanus, R.; Štubňa, J.; Jungmannová, K. Frankamenite as an ornamental gem material. *J. Gemmol.* **2020**, *37*, 132–133. [CrossRef]
35. Zhang, R.X.; Yang, S.Y. A mathematical model for determining carbon coating thickness and its application in electron probe microanalysis. *Microsc. Microanal.* **2016**, *22*, 1374–1380. [CrossRef] [PubMed]
36. *Bruker APEX2*, version 2.0-2; Bruker AXS Inc.: Madison, WI, USA, 2007.
37. *Bruker SAINT*, version 6.0; Bruker AXS Inc.: Madison, WI, USA, 2007.
38. Sheldrick, G.M. *SADABS, Program for Empirical Absorption Correction of Area Detector Data*; University of Göttingen: Göttingen, Germany, 2003.
39. Sheldrick, G.M. *XPREP*, version 2008/2; Bruker-AXS: Madison, WI, USA, 2008.
40. Betteridge, P.W.; Carruthers, J.R.; Cooper, R.I.; Prout, K.; Watkin, D.J. Crystals version 12: Software for guided crystal structure analysis. *J. Appl. Cryst.* **2003**, *36*, 1487. [CrossRef]
41. Copper, R.I.; Gould, R.O.; Parsons, S.; Watkin, D.J. The derivation of non-merohedral twin laws during refinement by analysis of poorly fitting intensity data and the refinement of non-merohedrally twinned crystal structures in the program CRYSTALS. *J. Appl. Cryst.* **2002**, *35*, 168–174. [CrossRef]
42. Kaneva, E.V.; Shendrik, R.Y.; Radomskaya, T.A.; Suvorova, L.F. Fedorite from Murun alkaline complex (Russia): Spectroscopy and crystal chemical features. *Minerals* **2020**, *10*, 702. [CrossRef]
43. Balić-Žunić, T.; Makovicky, E. Determination of the centroid or 'the best centre' of a coordination polyhedron. *Acta Crystallogr.* **1996**, *B52*, 78–81. [CrossRef]
44. Balić-Žunić, T.; Vicković, I. IVTON—Program for the calculation of geometrical aspects of crystal structures and some crystal chemical applications. *J. Appl. Cryst.* **1996**, *29*, 305–306. [CrossRef]
45. Breese, N.E.; O'Keeffe, M. Bond-valence parameters for solid. *Acta Cryst.* **1991**, *B47*, 192–197. [CrossRef]
46. Gagnè, O.C.; Hawthorne, F.C. Comprehensive derivation of bond-valence parameters for ion pairs involving oxygen. *Acta Cryst.* **2015**, *B71*, 562–578. [CrossRef]
47. Momma, K.; Izumi, F. VESTA 3 for three-dimensional visualization of crystal, volumetric and morphology data. *J. Appl. Crystallogr.* **2011**, *44*, 1272–1276. [CrossRef]
48. Hohenberg, P.; Kohn, W.J.P.R. Density functional theory (DFT). *Phys. Rev.* **1964**, *136*, B864. [CrossRef]
49. Kresse, G.; Furthmüller, J. Efficient iterative schemes for ab initio total-energy calculations using a plane-wave basis set. *Phys. Rev. B* **1996**, *54*, 11169. [CrossRef] [PubMed]
50. Perdew, J.P.; Burke, K.; Ernzerhof, M. Generalized gradient approximation made simple. *Phys. Rev. Lett.* **1996**, *77*, 3865. [CrossRef] [PubMed]
51. Kaneva, E.; Bogdanov, A.; Shendrik, R. Structural and vibrational properties of agrellite. *Sci. Rep.* **2020**, *10*, 15569. [CrossRef]

52. Dokuchits, E.Y.; Jiang, S.-Y.; Stepanov, A.S.; Zhukova, I.A.; Radomskaya, T.A.; Marfin, A.E.; Vishnevskiy, A.V. Geochemistry of Ca-(K)-(Na) silicates from charoitites in the Sirenevyi Kamen gemstone deposit, Murun Complex, Eastern Siberia. *Ore Geol. Rev.* **2022**, *143*, 104787. [CrossRef]
53. Hoppe, R.; Voigt, S.; Glaum, H.; Kissel, J.; Müller, H.P.; Bernet, K. A new route to charge distributions in ionic solids. *J. Less-Common. Met.* **1989**, *156*, 105–122. [CrossRef]
54. Nespolo, M.; Ferraris, G.; Ohashi, H. Charge distribution as a tool to investigate structural details: Meaning and application to pyroxenes. *Acta Crystallogr.* **1999**, *B55*, 902–916. [CrossRef]
55. Renner, B.; Lehmann, G. Correlation of angular and bond length dis tortions in TO_4 units in crystals. *Z. Kristallogr.* **1986**, *175*, 43–59. [CrossRef]
56. Robinson, K.; Gibbs, G.V.; Ribbe, P.H. Quadratic elongation: A quantitative measure of distortion in coordination polyhedra. *Science* **1971**, *172*, 567–570. [CrossRef]
57. Shannon, R.D. Revised effective ionic radii and systematic studies of interatomic distances in halides and chalcogenides. *Acta Cryst.* **1976**, *A32*, 751–767. [CrossRef]
58. McCusker, L.B.; Liebau, F.; Engelhardt, G. Nomenclature of structural and compositional characteristics of ordered microporous and mesoporous materials with inorganic hosts. *Pure Appl. Chem.* **2001**, *73*, 381–394. [CrossRef]
59. Cadoni, M.; Ferraris, G. Synthesis and crystal structure of $Na_2MnSi_4O_{10}$: Relationship with the manaksite group. *Rend. Fis. Acc. Lincei* **2011**, *22*, 225–234. [CrossRef]
60. Libowitzky, E. Correlation of O–H stretching frequencies and O–H. . .O hydrogen bond lengths in minerals. *Monatsh. Chem.* **1999**, *130*, 1047–1059. [CrossRef]
61. Beckenkamp, K.; Lutz, H.D. Lattice vibration spectra Part LXXII. OH stretching frequencies of solid hydroxides—Correlation with structural and bonding data. *J. Mol. Struct.* **1992**, *270*, 393–405. [CrossRef]
62. Bogdanov, A.; Kaneva, E.; Shendrik, R. New insights into the crystal chemistry of elpidite, $Na_2Zr[Si_6O_{15}]\cdot 3H_2O$ and $(Na_{1+y}Ca_x\square_{(1-x-y)})_{\Sigma=2}Zr[Si_6O_{15}]\cdot(3-x)H_2O$, and ab initio modeling of IR spectra. *Materials* **2021**, *14*, 2160. [CrossRef]
63. Kolesov, B.A.; Boldyreva, E.V. Difference in the dynamic properties of chiral and racemic crystals of serine studied by raman spectroscopy at 3−295 K. *J. Phys. Chem. B* **2007**, *111*, 14387–14397. [CrossRef]
64. Kaneva, E.; Bogdanov, A.; Radomskaya, T.; Belozerova, O.; Shendrik, R. Crystal-chemical characterizationand spectroscopyof fluorcarletonite and carletonite. *Mineral. Mag.* **2023**, *87*, 356–368. [CrossRef]
65. Kaneva, E.; Shendrik, R.; Mesto, E.; Bogdanov, A.; Vladykin, N. Spectroscopy and crystal chemical properties of $NaCa_2[Si_4O_{10}]F$ natural agrellite with tubular structure. *Chem. Phys. Lett.* **2020**, *738*, 136868. [CrossRef]

Disclaimer/Publisher's Note: The statements, opinions and data contained in all publications are solely those of the individual author(s) and contributor(s) and not of MDPI and/or the editor(s). MDPI and/or the editor(s) disclaim responsibility for any injury to people or property resulting from any ideas, methods, instructions or products referred to in the content.